Spatially correlated microthermography maps threshold temperature in laser-induced damage

Michael L. Denton
Gary D. Noojin
Michael S. Foltz
Clifton D. Clark III
Larry E. Estlack
Benjamin A. Rockwell
Robert J. Thomas

SPIE

Spatially correlated microthermography maps threshold temperature in laser-induced damage

Michael L. Denton,[a] **Gary D. Noojin,**[a] **Michael S. Foltz,**[a] **Clifton D. Clark III,**[a] **Larry E. Estlack,**[b] **Benjamin A. Rockwell,**[c] **and Robert J. Thomas**[c]
[a]TASC, Inc., Biomedical Sciences and Technology Department, San Antonio, Texas 78235
[b]Conceptual MindWorks, Inc., San Antonio, Texas 78228
[c]Air Force Research Laboratory, 711 HPW/RHDO, 2644 Louis Bauer Drive, Brooks City-Base, Texas, 78235

Abstract. We measured threshold temperatures for cell death resulting from short (0.1–1.0 s) 514-nm laser exposures using an *in vitro* retinal model. Real-time thermal imaging at sub-cellular resolution provides temperature information that is spatially correlated with cells at the boundary of cell death, as indicate by post-exposure fluorescence images. Our measurements indicate markedly similar temperatures, not only around individual boundaries (single exposure), but among all exposures of the same duration in a laser irradiance-independent fashion. Two different methods yield similar threshold temperatures with low variance. Considering the experimental uncertainties associated with the thermal camera, an average peak temperature of $53 \pm 2\,°C$ is found for laser exposures of 0.1, 0.25, and 1.0 s. Additionally, we find a linear relationship between laser exposure duration and time-averaged integrated temperature. The mean thermal profiles for cells at the boundary of death were assessed using the Arrhenius rate law using parameter sets (frequency factor and energy of activation) found in three different articles. © *2011 Society of Photo-Optical Instrumentation Engineers (SPIE)*. [DOI: 10.1117/1.3548881]

Keywords: laser-induced damage; cells; thermal effects.

Paper 10510PR received Sep. 16, 2010; revised manuscript received Dec. 10, 2010; accepted for publication Jan. 6, 2011; published online Mar. 11, 2011.

1 Introduction

The difference between delivering an acute thermal dose that overtly kills a cell, from one that induces a protective heat shock response can be the difference between successful killing of cancerous cells and aggressive tumor relapse. Like optical properties[1] and molecular imaging technologies,[2] which show promise in distinguishing normal from neoplastic cells, variations in thermal response kinetics could also prove valuable. Correlation of temperature history with cellular responses for short non-isothermal laser exposures has been a longstanding challenge.[3] Future surgical procedures will likely employ intraoperative thermal imaging[4] with feedback control of laser dose based on known cell-specific thermal damage kinetics[5,6] to ensure desired therapeutic effects. However, predicting cellular outcomes based on laser dose kinetics is inherently difficult. Prediction requires computational modeling of thermal deposition and heat distribution within a given tissue type. In some instances, thermal and optical properties of tissues are unknown, thus, leading to inferences about absorption. Even if tissue properties and accurate models are available, if the thermal sensitivity (threshold temperature) of a cell is unknown the predictive power of the computation is in question.

Various methods of measuring and estimating temperatures resulting from laser exposure have been described. Early in the field of laser bioeffects, temperature measurements were taken in response to laser irradiation at 488 nm using surgically implanted microthermocouples in the rabbit[7] and monkey[8] eye. More recently, thermocouples were used to measure temperatures of laser-irradiated prostate tissue.[9] Another single-point method for measuring temperature is to focus thermal emission onto a mercury cadmium telluride detector.[10] However, single-point analyses cannot provide complete two-dimensional descriptions of heat distribution within a tissue or cell layer and computational models are used to compensate for this inadequacy.[7,8,10] Magnetic resonance thermometry (MRT) has been shown to provide reliable temperature measurements during *in vivo* interstitial laser coagulation of the canine prostate.[11] Unfortunately, the temporal and spatial resolution of MRT is insufficient for determining thermal history of individual cells for short thermal exposures. There is a relatively new method of analyzing damage responses of single cells to laser exposure,[12] but it involves spectral evaluations rather than measuring temperature.

A superior method for measuring temperature distribution is one that provides both temporal and spatial information, such as full-frame thermal microscopy (thermography).[4] Choi et al.,[13] used high-speed thermography to capture ablative responses of skin when exposed to short pulses from a clinical CO_2 laser, but no threshold of tissue damage was reported. Thermography was also used to follow temperature rise during laser exposures of cartilage material at powers consistent with clinical reshaping.[14] In that study, fluorescence damage detection using confocal microscopy identified regions of dead chondrocytes but there was no correlation between temperature history and threshold cellular death.

Here, threshold temperatures for cellular damage were determined in response to short photothermal exposure, taking advantage of spatial correlations between high-magnification

Address all correspondence to: Robert J. Thomas, AFRL/RHDO, Air Force Research Laboratory, 2624 Louis Bauer Drive, Brooks City-Base, TX 78235-5214. Fax: 210-536-3903; E-mail: robert.thomas@brooks.af.mil

thermal images (microthermography) and post-exposure fluorescence damage images. Our spatially-resolved method differs from traditional studies using threshold laser irradiance in that we measure temperatures at the boundary between live and dead cells following laser exposures of suprathreshold irradiances. Cells at this boundary of cell death are considered to be equivalent to each other in that they have been subjected to the threshold dose of temperature history needed for damage at 1 h post-exposure. The method was illustrated using 514-nm laser exposures of an existing *in vitro* retinal model[15] that contained pigmentation to enhance laser absorption. Our results indicate that cells at the boundary of cell death experienced the same peak temperature (~53 °C) at the end of laser exposures of 0.1, 0.25, and 1.0 s, regardless of laser irradiance. Additionally, we found a linear relationship between laser exposure duration and threshold time-averaged integrated temperature rise. We propose that the microthermography approach will enable the exploration of differences in thermal susceptibility between normal and neoplastic cells using such diverse techniques as viability and apoptosis staining, immunohistochemistry, reporter gene expression, and *in situ* hybridization.

2 Materials and Methods

2.1 Experimental Setup

The schematic for the experimental setup is shown in Fig. 1. The 514-nm output of a large-frame argon laser (Coherent, INNOVA 200) was used to expose cells for durations of 0.1, 0.25, or 1.0 s in 48-well microtiter plates (one exposure/well). The laser beam was launched into a 0.3-mm multimode fiber. The tip of the fiber was relay-imaged to the sample plane as a flat top 0.93 mm-diam image. Thus, the magnification of the dual-lens imaging system shown in Fig. 1 (L2 and L3) was 3.1:1. A final turning mirror was placed beneath the 100-mm IR lens and was out of focus of the thermal camera. Laser exposures were carried out in a custom-built plexiglas enclosure[16] that maintained ambient temperature and relative humidity at 35 ± 1°C and 62 ± 4%,
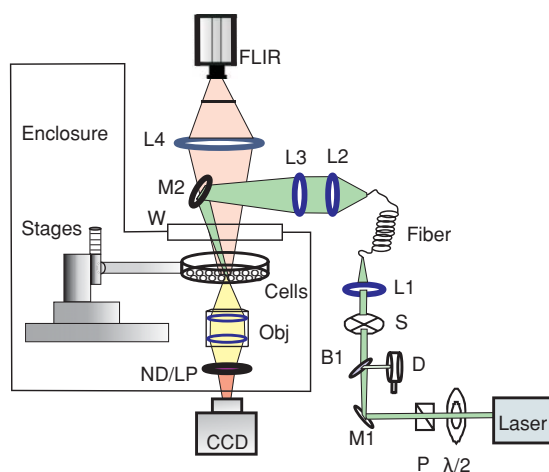
respectively. Culture dishes were suspended using an aluminum holder attached to a micrometer (*z* dimension), which in turn was affixed to a computer-driven *x-y* translational stage assembly.
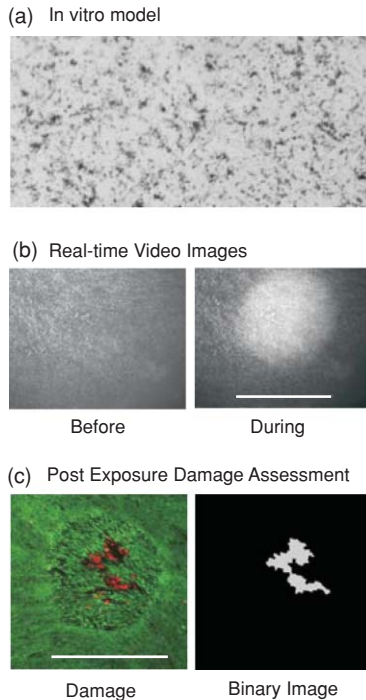
The plexiglas enclosure was designed with a ledge, fitted with a MgF$_2$ optical window, to enable viewing at 3–5 μm with a thermal camera (FLIR Systems, ThermoVision SC6000, MWIR, InSb). We focused the sample plane at 3.1-fold magnification via a 100-mm IR lens (Janos, ASIO, 100 mm, F/2.3, MWIR), resulting in an effective pixel pitch of 8.12 μm. In order to ensure the thermal camera was focused on the retinal pigment epithelial (RPE) cells, we established a common focal plane with a 5× infinity-corrected, long-working distance, MPLAN APO microscope objective (Mitutoyo) located beneath the sample plane. The sample was placed in focus with the CCD camera using a *z*-field micrometer. Light from the microscope objective was focused to a Hamamatsu ORCA 100 CCD camera (effective pixel pitch of 1.36 μm/pixel), and a long-pass filter was placed between the microscope objective and CCD camera to attenuate the laser light.

2.2 Calibration of Thermal Camera

A portable NIST-traceable blackbody source (Mikron model M316) was used for calibration of the forward-looking infrared (FLIR, Boston, Massachusetts) camera with an accuracy of ± 0.5% of temperature reading ± 1°C (e.g., 50°C ± 1.25%). The thermal camera was calibrated using the blackbody placed in the location that cells were exposed using a temperature range of 30–120 °C. The resulting calibration curve was verified as accurate under experimental conditions by repeating the measurements from 40–120ºC when the exposure enclosure was fully equilibrated for temperature and humidity. The experimental setup was not altered after a calibration curve was generated. As a short-term calibration, we adjusted the camera offset before each laser exposure based on the temperature of a painted (flat black) aluminum plate with known emissivity. The temperature of the aluminum plate was that of the interior of the exposure enclosure (35 ± 1ºC) and was verified by an inserted thermocouple.

2.3 Laser Exposures and Damage Assessment

We used a previously described *in vitro* retinal model utilizing RPE cells as the absorptive tissue in laser exposure experiments.[15] Cultured hTERT-RPE1 cells (ATCC #CRL-4000) were seeded into 48-well microtiter plates (BD Biosciences Falcon, Franklin Lakes, New Jersey) at a density of 70,000 per well two days prior to laser exposure, and previously isolated melanosome particles (MPs) were added the following day to an average density of 160 MPs/cell (based on one cell doubling). Figure 2(a) shows the typical pigmentation distribution within cellular monolayers at the time of laser exposure. Before photothermal exposure, cultures were twice rinsed with pre-warmed Hank's balanced salt solution (HBSS) and 0.1 mL of warmed HBSS was applied to each well. Our method of liquid handling employed the use of a piece of small-diameter tubing held into place along the side of the culture well with an adapter that did not hinder laser delivery or imaging. The opposite end of the tubing was connected to a small syringe. Immediately prior to (and after) each laser exposure, the HBSS

Fig. 1 Experimental design. Experimental setup showing laser beam delivery and dual imaging components (CCD and FLIR cameras). L: lens, M: mirror, ND/LP: neutral density/long-pass filters, W: optical window (MgF$_2$), S: mechanical shutter, B: beamsplitter, λ/2: half-wave plate, P: polarizing beam splitter, D: power detector.

Fig. 2 Images before, during and after laser exposure. (a) Transmitted-light micrograph (25× magnification) of a typical *in vitro* sample used in laser exposures. (b) Video images (5× magnification) of cells prior to and during laser exposure using the CCD camera in Fig. 1. The bright region in the image during exposure indicates the laser exposure site. (c) Detection of cell death 1-h post exposure. The dual fluorescence images (4× magnification) are shown as an overlay. The composite (dual fluorescence) image was used to generate the binary image for both identifying thermal pixels at the boundary of death and in calculating the area of damage caused by the 0.1-s laser exposure in Fig. 1(b) (120 W cm²). All spatial bars represent 0.93 mm.

buffer was completely removed (and replaced) by action of the syringe. We estimate the cells were without liquid for ≤ 25 s during this process. Similar to using multiple animals for *in vivo* studies, we captured cell heterogeneities by collecting data over the course of multiple days, each time adhering to the strict cell culture protocol (plating cells on day 1, pigmenting on day 2, and exposure to laser on day 3).

We used a computer program developed in LabVIEW (National Instruments) for automation of the following sequence of events for data collection: movement of a 48-well plate to a predetermined well location, initialize thermal (800 fps) and video (9 fps) camera acquisitions (both were time-stamped from the same Inter-Range Instrumentation Group time-code generator), open and close mechanical shutter for desired duration of laser exposure, and end acquisition by both cameras. Figure 2(b) gives an example of video images before and during laser exposure of cells.

After exposures, the HBSS was replaced with 0.3 mL of warmed growth medium and cells were transferred to a 37°C incubator for 1 h.[15] Cells were stained for viability [Fig. 2(c)] at 37°C with 0.1 mL HBSS containing 1.7 μM calcein-AM and 1.4 μM ethidium homodimer 1 (Molecular Probes) for 10–15 min. We obtained fluorescence images of stained cells using an ORCA II CCD camera (Hamamatsu) attached to a

CK40 inverted microscope (Olympus) with a 4× objective (2.18 μm/pixel).

2.4 Data Processing

2.4.1 Thermal data

The only way to achieve the correlations between the spatially-resolved damage and thermal images needed to determine temperature of cells at the boundary of cell death is to overlay them with accurate registration, identify boundary pixels common to both images, and then extract thermal information from the FLIR movies. Validation of our results depends on this step; thus, we have described our method of image overlay in detail. We developed a program in LabVIEW to analyze the thermal movie files generated by the FLIR proprietary ThermaCAM RDac data acquisition program. In order to correlate the multiple thermal profiles generated within exposure durations, it was important to identify the first frame the laser was applied to the cells. This was achieved by visually inspecting the thermal window [Fig. 3(a)] while moving the thermal movie scroll bar [Fig. 3(i)]. We verified laser exposure duration by tracking the hottest pixel per frame in the temperature scale bar [Fig. 3(ii)] while varying the current frame number [Fig. 3(iii)] to values on either side of the expected last frame. The software allows the extraction of many temperature metrics, such as temperature (and time-averaged temperature) as a function of time for single pixels,
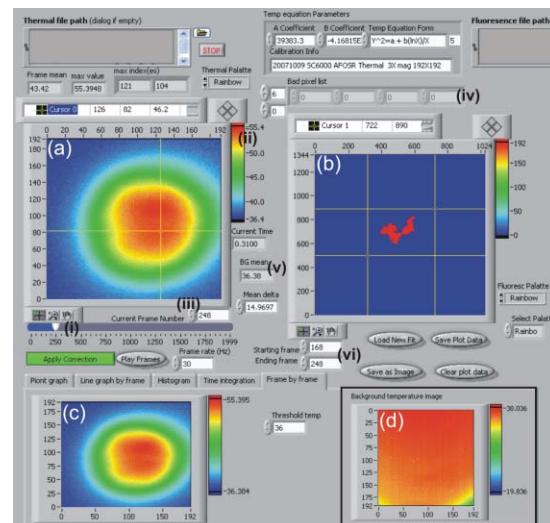
Fig. 3 Thermal data analysis. Thermal data (all seven raw data files generated by RDAC of FLIR Systems) were analyzed by a modified LabVIEW program for easy interface. (a) Background-corrected full-frame thermal image representing frame 248 (iii) of the thermal movie generated during the laser exposure shown in Fig. 2. The slider (i) was used to find the first and last frames for which the laser was applied to sample cells. Alternatively, individual frame numbers can be input (i) or data extracted in (c) for a given start and stop frame (vi). Mean background temperature (v) was displayed. Temperature value of the hottest pixel of a frame is given in (ii) and known aberrant pixels can be listed (iv) and omitted from analyses. (b) Binary image of damage [see also Fig. 2(c)]. (c) Full-frame image of frame designated in (iii). When the "Time Integration" tab of (c) is chosen, the analysis in window (c) would be time-integrated temperature (full-frame). (d) Full-frame temperature background, as calculated by averaging each pixel over the first 50 frames of thermal movie.

horizontal/vertical lines, or entire thermal frames. Alternatively, we extracted thermal data for a region of interest (ROI) mask that represented the cells at the boundary of cell death (see below).

To calculate background temperatures, we averaged the values of each pixel over the first 50 frames of the movie, which was prior to the opening of the laser shutter. A full-frame representation of the temperature background is shown in Fig. 3(d). The temperature maps shown in Fig. 3(a) were the result of a two-step correction process. The raw thermal frame was corrected for background by subtracting the "background temperature image" [Fig. 3(d)]. Then, the mean temperature ("BG mean") of the "background temperature image" [Fig. 3(v)] was added to each pixel to provide the spatially-resolved corrected temperature map shown in Fig. 3(a). To report threshold temperature values, we obtain temperature rise values by subtracting the "BG mean" values and then added the 35 ($\pm$1)°C ambient temperature of the plexiglass exposure enclosure.

The software ["Time integration" tab of Fig. 3(c)] also enabled us to determine background-corrected time-averaged integrated temperatures (T_{int}) at each pixel over any specified time interval [Fig. 3(vi)]. This function multiplies the sum of all the temperature values within the specified time interval by the time interval between frames (0.00125 s for 800 fps). To normalize all our T_{int} values, we subtracted the product of the BG mean value and the time interval chosen [Fig. 4(vi)], which gave background-corrected T_{int} rise values.

2.4.2 *Identifying threshold temperature for cell damage*

Damage area method. For each laser exposure that caused identifiable damage, we generated a damage ROI from the composite (calcein and ethidium homodimer image overlay) fluorescence damage image [Fig. 2(c)] using the histogram algorithm of the SimplePCI software package (Compix, Inc). The area of each ROI was extracted, and the binary images representing the ROIs [Figs. 2(c) and 3(b)] were saved and used to identify registration parameters for subsequent image overlays. For each spatially-resolved background-corrected temperature map [Fig. 3(c)], the constant-temperature contour line that defined an area equal to the laser-damaged area was found. When using the last frame the laser was on, this method provided a temperature value associated with the boundary of cell death (threshold) at the end of the laser exposure.

In Fig. 4, the same example exposure used in Figs. 2 and 3 was used to show specifically how we performed our analysis. By setting the current frame number [Fig. 3(iii)] to the last frame the laser was on (248 in this example), the thermal image shown in Fig. 3(c) was converted to a binary image and displayed in Fig. 4(b). The binary thermal image in Fig. 4(b) had been thresholded such that the minimum temperature in the contour map was set by the value in the "Thermal threshold" box. We manually adjusted the value in the "Thermal threshold" box such that the "Thermal image area" value equals the area damaged by the laser ("Fluorescence area"). The background-corrected thermal threshold giving rise to matching image areas (shown as 53.9957°C in this case) was the threshold temperature (rounded to 54°C) based on damage area. Changing the threshold temperature by 0.01°C changed the area of the temperature contour image by 2.8%.
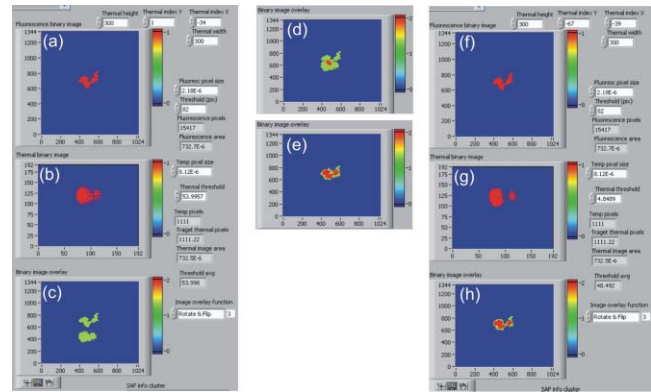

Fig. 4 Damage threshold temperature and time-integrated temperature using damage area. Using the same example exposure shown in Figs. 2 and 3 (a–e), damage threshold temperature and (f–h) damage threshold time-integrated temperature were determined. **(a)** Binary image of damage for overlay. **(b)** Binary image of Fig. 3(c) when "Thermal threshold" (to right of window) is set such that "Fluorescence area" matches "Thermal image area." **(c–e** Progression of image overlay process for threshold temperature. The overlay parameters ["Image overlay function" near (c) and (h), and the values for "Thermal index *X*" and "Thermal index *Y*" near (a) and (f)] are important for future overlays between thermal images and boundary of death ROI masks. **(f–h)** Analysis similar to (a–e) using threshold time-integrated temperature.

Alternatively, when the "Time integration" function in Fig. 3(c) was used, a binary image representing background-corrected time-averaged integrated temperature is generated [Fig. 4(g)]. After matching the areas of the binary maps [Figs. 4(f) and 4(g)], the T_{int} value (shown as 4.8489°C s in this example) was the threshold value based on damage area. Changing the threshold T_{int} by 0.01°C s changed the area of the T_{int} binary image by 25%. To obtain the threshold T_{int} rise values we report here, we subtracted the product of the "BG mean" (36.38°C) and the time interval (0.1 s) to get 1.211°C s.

Damage boundary method. To identify pixels of a thermal movie corresponding to cells at the boundary of death, we generated a boundary image mask from the fluorescence damage image and overlaid it with a thermal movie image that had been resampled and rotated appropriately. The spatial resolution [(8.12 μm)^2] of the 192×192 pixel array of the thermal images was resampled to match that [(2.18 μm)^2] of the 1024×1344 pixel array of the fluorescence images. After resampling, the number of replicate thermal pixels was ~14 (8.12^2/2.18^2) and the thermal image was approximately 714×714 pixels.

Figures 4(c)–4(e) illustrate progress during image overlay and alignment until maximum overlap between the images [Fig. 4(e)] was achieved. The LabVIEW program adds the two binary images [Figs. 4(a) and 4(b)], each having pixel values of 0 (blue) or 1 (green), generating red color for overlapping portions (value of 2). The orientation of the two images required the background-corrected binary thermal image to be rotated and flipped relative to the fluorescence image using the "Image overlay function" utility at the right of window C. Values in the "Thermal index *Y*" and "Thermal index *X*" windows [Figs. 4(a) and 4(f)] were adjusted dynamically until maximum overlap (red) occurred. The thermal index values were recorded for each exposure data set to enable subsequent overlaying of boundary image masks with their corresponding background-corrected thermal movie frames. Similarly, overlay
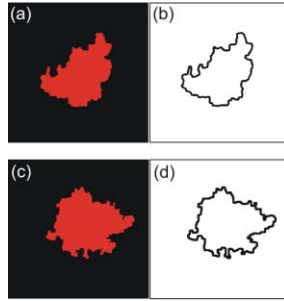
Fig. 5 Examples of boundary of cell death regions of interest. Fluorescence damage images ((a) and (c)) were used to generate single-pixel wide ROI masks representing cells at the boundary of cell death.

of a binary damage image [Fig. 4(f)] with its corresponding background-corrected T_{int} binary image [Fig. 4(g)] provided an analysis for best-fit overlay parameters [Fig. 4(h)].

We created image masks for the boundary damage by selecting the single layer of pixels just outside of the binary damage images using the edge algorithm of the SimplePCI software package. Examples of some damage images and their boundary mask images are given in Fig. 5. Using the optimum overlay parameters determined for each data set as described above, boundary mask images were overlaid with corresponding thermal images and a boundary ROI of the thermal image identified. The data extracted from the boundary ROI for each thermal movie frame included the number of pixels in the ROI, the frame number, and the mean temperature with standard deviation. Data were assembled into spreadsheet format for analyses.

3 Results and Discussion

3.1 *Threshold Temperature*

The conventional usage of the term, "threshold temperature" in laser damage studies implies measurement of a lesion that is minimal in size that does not enlarge with extended time post-exposure. The measurement may be in the form of single-point temperature assessed in the center of irradiated tissue, or a simulated temperature based on both the threshold laser irradiance and tabulated optical properties of the target tissue. Most spatially-resolved methods of assessing damage after a suprathreshold exposure (e.g., fluorescence microscopy) will identify a boundary, demarking damaged (inside) and non-damaged (outside) cells. A complementary spatially-resolved temperature measurement would take full advantage of the spatially-resolved damage information, and could be used to identify threshold temperature at the boundary of cell damage. This combined method would provide a means of uncoupling damage from laser irradiance, and correlate the damage directly with temperature dose (temperature history). The method we present here provides both the spatially-resolved damage and temperatures required for determining threshold temperature as defined at the boundary of cell death. The only caveat for this correlation is devising a way to overlay and register the damage and thermal images, which we have done with a novel computer program written in LabVIEW.

To illustrate how our threshold temperature method differs from a conventional irradiance method, we refer to Fig. 6, where
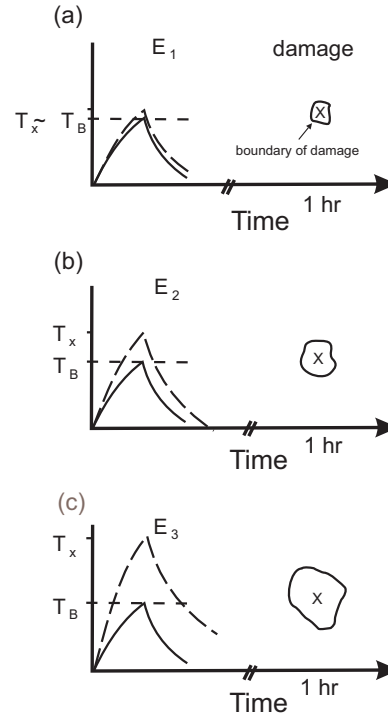
Fig. 6 Definition of threshold temperature at the boundary of cell death in response to photothermal damage mechanism. Artificial data are shown to illustrate the relationship between the temperature at the center of a laser irradiated region and the temperature at the boundary of cell death. (a) Near-threshold irradiance yields a small area of damage 1 h post exposure and the temperature at the boundary (T_b) is only slightly lower than that produced at the center of the exposure site (T_X). (b–c) As laser irradiance is increased above threshold ($E_1 < E_2 < E_3$), T_X rises due to increased absorption. However, T_B remains constant for the same damage assessment times post exposure.

the example laser exposure parameters are expected to generate damage by thermal mechanisms. Figure 6(a) illustrates that at near-threshold irradiance (E_1) the temperature value at the boundary of cell death (T_B) is near the temperature value (T_X) at the center of the exposure site (X) at the time of damage assessment. At threshold irradiance, $T_x = T_B$, and the damaged area is a minimal lesion. With suprathreshold laser irradiances [Figs. 6(b) and 6(c)], the thermal and spatial separations between T_B and T_X are greater than at the threshold irradiance, with T_B remaining constant while T_X increases with increasing irradiance. We believe spatially-resolved methods measuring temperature threshold at the damage boundary have greater utility than those using single-point temperature measurements because the laser exposure irradiance needs not be precisely at the threshold.

The goal of this study was to reasonably measure the temperature at the boundary of cell death at a given time post exposure. We chose 1h post-exposure times because that was part of the designed *in vitro* retinal model previously characterized.[15] Additionally, we wanted to determine how consistently cells died at the threshold temperature within a given exposure duration while varying irradiance above the threshold value, and how this boundary temperature varied across exposure durations. Thus, the irradiances used in the three exposure durations were, for the most part, not meant to be indicative of the threshold requirement for minimal lesions, only that they provided a wide range

of damage sizes and shapes within the RPE cell monolayer. Note that if a laser wavelength generating bulk water heating were used, or if a water bath could be used to generate a thermal profile similar to that generated by a laser, the temperature distribution would be more homogeneous across the tissue and the size and shape of damage would be expected to be more uniform than in our melanin-based heating.

To obtain temperature information at the cellular level, we acquired real-time thermal and subsequent viability images at magnifications that resolve individual cells. The $4\times$-objective used for damage assessment by conventional fluorescence microscopy easily fulfilled this requirement (2.18 μm/pixel), while the magnification of our thermal microscope provided an effective pixel pitch of $\sim$8 μm/pixel. The size and shape of individual cultured RPE cells varied dramatically (typically 20–40 μm); however, each nucleus was consistently spherical with an average diameter of $\sim$12 μm. We therefore conclude that our analysis provided approximately two thermal pixels per RPE cell.

Figure 7 highlights the importance of spatially resolving temperature variations of the cell monolayer during laser exposure. Here, we continue using the same example 0.1-s exposure that was shown in Fig. 2. The temporal thermograms [Fig. 7(a)] and the fluorescence damage image [Fig. 7(b)] are presented in the same orientation for comparison. The 40–80-ms thermograms indicate two distinct elongated regions that correlate with the damaged areas. The separation of temperature occurs early in

the laser exposure but does not persist during the cooling phase after the laser is turned off. These results suggest an uneven absorption during laser exposure, which then resulted in a similar pattern of cell death. The non-uniform distribution of pigment [refer to Fig. 2(a)] is a likely cause of the non-uniform heating in the cell monolayer.

An overview of the two methods used to determine peak threshold temperature at the boundary of cell death is given in Figs. 7(b) and 7(c). The damage area method [Fig. 7(b)] uses the thermogram corresponding to the last frame in the laser sequence, representing peak temperatures at each pixel, to compare temperature contour area to the area damaged by the laser 1-h post exposure (binary black and white image). The outer edge of the threshold thermogram for this example was 52.6 °C. The overlay of the threshold thermogram and the fluorescence damage image revealed a close proximity between the outer edge of the threshold thermogram and the boundary of cell death. Table 1 summarizes our threshold peak temperature values across the three laser exposure durations using the damage area method.

Figure 7(c) outlines the damage boundary technique for the specific 0.1-s exposure example. The specific damage boundary ROI was used to overlay a thermal frame to generate the corresponding thermal ROI [refer to Figs. 4(c) and 4(e)], from which the thermal pixels at the boundary of death were identified. The list of thermal pixels corresponding to the boundary ROI allowed us to extract the temperature of the cells at the boundary
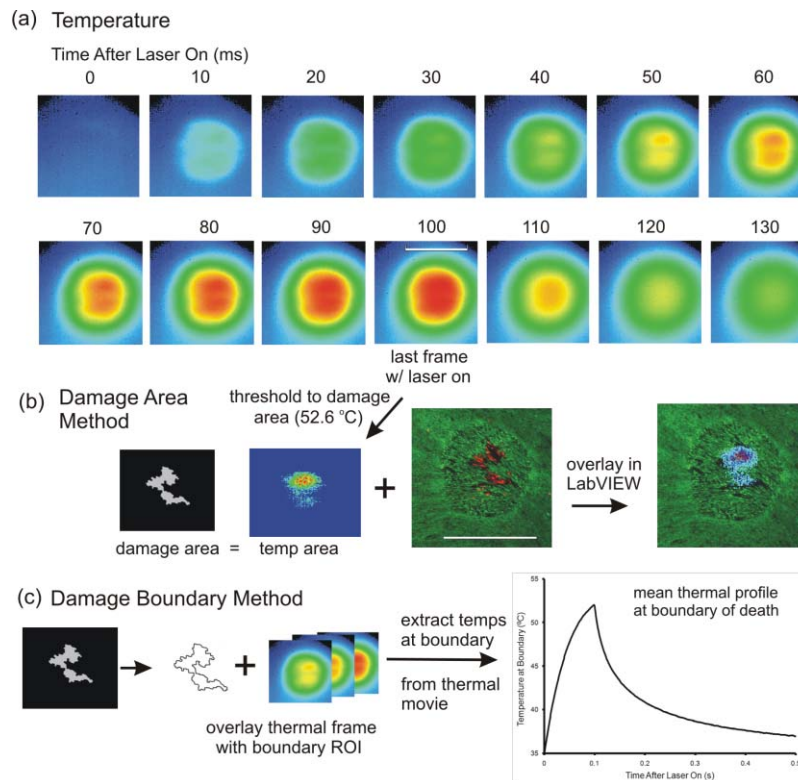
Fig. 7 Determining threshold temperature for *in vitro* laser-induced cell death. **(a)** Periodic thermograms during the example 0.1-s exposure. **(b)** Diagram of the damage area method, which uses the last frame for which the laser was applied to the cells. After determining the threshold temperature (described in Fig. 4), the thresholded thermogram was overlaid onto the fluorescence damage image to show similar boundaries. **(c)** Diagram of the damage boundary method, which identifies thermal pixels corresponding to cells at the boundary of cell death. Thermal profiles can then be constructed using the extracted temperature history.

Table 1 Thermal analyses of *in vitro* retinal model exposed to 514-nm laser.

Exposure duration	No. expos	Range of laser irrad (W/cm^2)	Equiv. pixels at boundary	Threshold T_{Peak}(°C)		Threshold T(°C)	Threshold T_{ave}(°C)
				Damage boundry	Damage area	Damage boundary	Damage area
0.10	16	102–178	5364	51.88 (0.33)[a]	52.21 (0.33)	1.126 (0.021)	46.26 (0.21)
0.25	21	80–150	6527	55.25 (0.17)	54.56 (0.19)	3.590 (0.024)	49.36 (0.10)
1.00	20	30–110	6666	51.26 (0.22)	51.25 (0.22)	13.80 (0.165)	48.80 (0.17)

[a]Standard error of the mean values.

of death during the course of the laser exposure. When the mean temperature of the boundary ROI (251 pixels, in this example) for each frame is plotted relative to the first thermal frame in which the laser was detected (heat generated), a combined thermal profile of all the cells at the threshold of cell death was generated [Fig. 7(c)]. Clearly, this method is superior to the damage area method because it provides temporal information about the temperatures experienced by the cells at the boundary of death. The threshold peak temperature is defined as the mean temperature of the boundary ROI in the last frame for which the laser was on, which was 51.9°C in this particular example.

Figure 8 shows the boundary ROI thermal profiles for each of the three exposure durations, both individually [Figs. 8(a)–8(c)] and as a combined mean threshold thermal profile representing the exposure durations [Fig. 8(d)]. It is important to note that each of the individual thermal profiles in Figs. 8(a)–8(c) represent the mean temperature of all the pixels at the boundary of cell death for that individual laser irradiance. When we averaged at each time point all the thermal profiles within each exposure duration, the resulting thermal profiles [Fig. 8(d)] were depicted with error bars (*y*-axis) representing the standard errors of the mean at each time point. The temperature and standard error of the mean for the final thermal frame the laser was on defines the threshold peak temperature at the boundary for each exposure duration, which are presented in Table 1.

Multiple noteworthy features of the microthermography data are evident in Table 1 and Figs. 7 and 8. Within each exposure duration data set, there were thousands of pixels identified as being at a boundary of cell death (Table 1). The number of pixels making up a given boundary ROI is determined by the size (circumference) of the laser damaged area, which was dependent on absorption (and heat generation) of the 514-nm laser light. We therefore had a variety of ROI shapes and sizes over the broad range of laser irradiances we used within exposure durations. Once the first frame of each thermal movie (relative to the laser on time) was used to compare thermal profiles (Fig. 8), our belief that all cells at the boundary of cell death must receive equivalent temperature histories was supported. The extremely low standard errors of the mean for each threshold thermal profile in Fig. 8(d) is a remarkable result, and is likely due both to a precision of the microthermography method and a narrowly regulated functional response in the RPE cells.

Although the two methods did not give the exact same threshold peak temperature for the specific example in Fig. 7, the two values (52.6°C versus 51.9°C) were within the uncertainty of the thermal camera measurement (± 1.5°C). In fact, all the threshold peak temperature values listed in Table 1 were within their respective standard errors of the mean of each other. We therefore propose that the threshold peak temperatures for all three exposure durations were statistically indistinguishable from each other. From the six values in Table 1, the overall mean threshold peak temperature is calculated to be 52.7 $\pm$ 0.71°C, which we will report as 53°C hereafter. Figure 8 also shows that even though the mean peak temperatures of the three exposure durations were essentially the same, the shapes of the mean thermal profiles varied. Most notable was the nearly steady-state temperature achieved by the end of the 1.0-s exposures.

The threshold value of 53°C is probably slightly lower than the actual temperature experienced by some cellular compartments within the cells at the boundary of death. For instance, localized temperatures around the small (about 1×1 μm) MPs within the cells were likely greater than the temperature measured by the thermal camera due to spatial averaging across the 8×8 μm pixels during the 1.25-ms camera integration time. We do not know how much greater the temperature was at individual MPs, and methods for measuring temperature at 1-μm resolution have not been reported. We do not expect cell death as the result of microcavition[17] because we used pulse widths ≥ 10 μs. However, temperatures greater than those measured by the FLIR camera could be achieved at subcellular structures and metabolic pathways, and thermal disruption at higher threshold temperatures of these functions could be responsible for cell death.

Another rationalization for a lower than-expected threshold temperature is attenuation of light (3–5 μm) imaged by the thermal camera. The most likely source for attenuation of heat to the camera would be the presence of aqueous liquid between the cells and the camera, such as incomplete removal of buffer covering the cells prior to laser exposure. We have determined that ≤ 3 μL of buffer remained at the end of liquid removal in preparation for microthermography. In our experiments, the height of 100 μL in the center of a well with cells (48-well plate) is $\sim$100 μm, thus, we expect the depth of buffer above the cells is determined by surface tension forces alone. Even
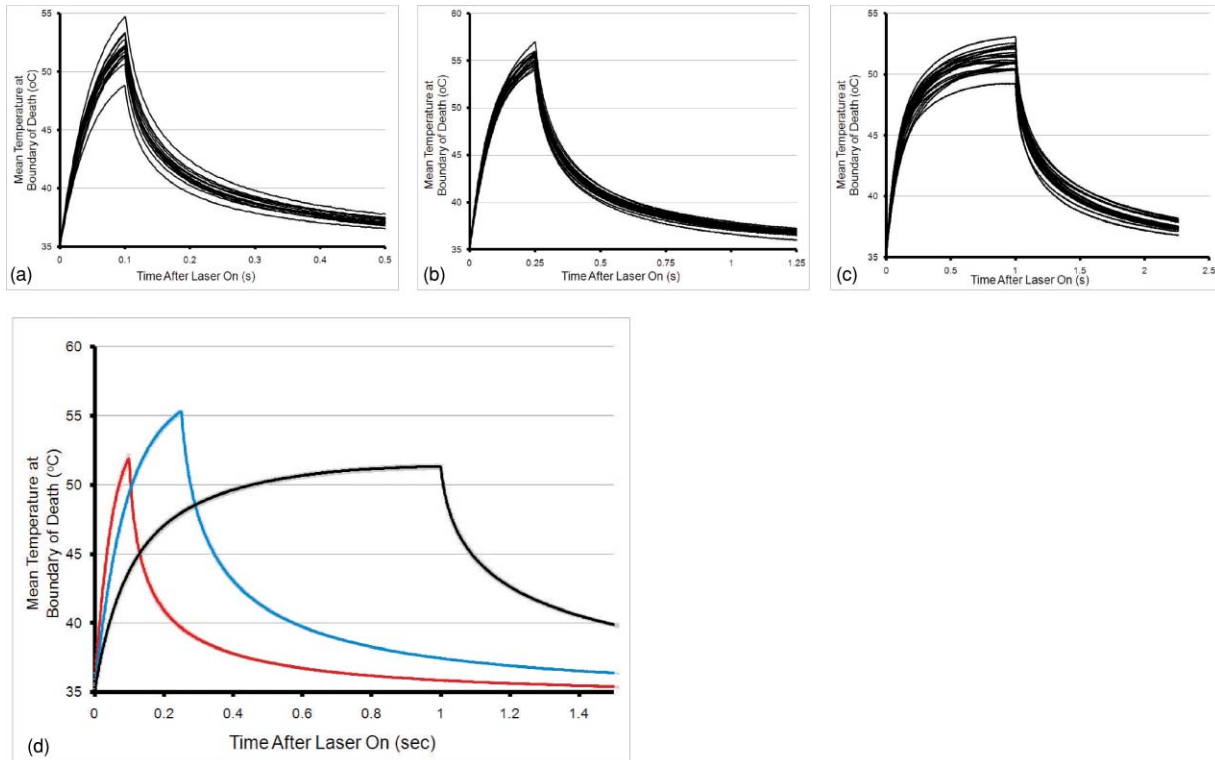
Fig. 8 Thermal profiles for cells at the boundary of cell death. Averaged thermal profiles at the boundary of cell death for *in vitro* exposures to **(a)** 0.1, **(b)** 0.25, and **(c)** 1.0 s. For each exposure duration, mean temperatures for all pixels within each boundary ROI were plotted as a function of time after the laser was applied to the cells. **(d)** The thermal profiles in (a-c) were averaged within each group and plotted as the overall thermal profiles for the laser exposures, showing standard error of the mean error bars.

though it is likely an overestimate, when we assume 7 μm of buffer existed above the cells at the time of laser exposure, the calculated thermal diffusion time (t = distance^2/4·thermal diffusivity)[18] was ~90 μs. This time interval is 14 times shorter than the integration time (1.25 ms) of the thermal camera, and because of this rapid thermal diffusion, the cell layer (~7 μm thick) and the very thin aqueous layer above it will be essentially in equilibrium as measured by thermography at 800 fps.

3.2 Damage Rate Process

The fact that we found no difference in the threshold (boundary) peak temperature for exposures of 0.1–1.0 s in our *in vitro* retinal model is inconsistent with current predictive models for thermal damage. The most common method for predicting laser-induced thermal damage is the Arrhenius integral damage model. A damage parameter, Ω, is related to the tissue temperature, $T(t')$, through the Arrhenius integral,

$$\Omega = A \int_0^\tau e^{\frac{-E_a}{RT(t')}} dt', \qquad (1)$$

where A and E_a represent the frequency factor (measured in secondes to the -1) and energy of activation (measured in Joules per molecules), respectively. R is the universal gas constant (8.31 J mol^{-1} K^{-1}). The two rate coefficients, A and E_a, must

be measured experimentally and their values will depend on the tissue type and method used for measuring damage. One complication inherent in the Arrhenius damage model is that it lacks a repair rate. This means that, practically, the range of integration can significantly alter the damage parameter, and that the model will always predict an accumulation of damage as a finite time at all temperatures, even those known not to cause damage (such as body temperature).

In some cases, the value of the damage parameter may correspond to a quantifiable amount of damage,[3, 19] but often a damage threshold is defined. The most common threshold used is where $\Omega = 1$. To determine A and E_a values that compute $\Omega = 1$, the temperature profile of a laser exposure that causes threshold damage (minimum lesion) must be obtained. If only the peak temperature of the exposure is recorded (single-point measurement), then several exposures must be conducted, and only the temperature profile from exposures causing minimal (threshold) damage can be used. Simanovskii, et al., have reported methods to obtain temperature profiles at the cell death boundary of an exposure, such that any exposure causing damage can be used in the analysis.[10] In their analysis, the peak temperature rise at the center of laser exposed site was measured and spatial temperature distribution was predicted using computer models. Temperature was not temporally extracted for cells at the death boundary,[10] and to our knowledge, data presented in this report are the first examples of thermal profiles directly measured at the boundary of cell death.

Table 2 Arrhenius modeling of *in vitro* data using three different sets of rate coefficients.

Exposure duration (s)	Polhamus[a]			Simanovskii[b]			Moussa[c]		
	Ω at τ	Scaling factor	Adjusted T_{peak} (°C)	Ω at τ	Scaling factor	Adjusted T_{peak} (°C)	Ω at τ	Scaling factor	Adjusted T_{peak} (°C)
0.10	0.003	1.53	61.1	0.406	1.62	62.6	5.4×10^5	3.5	94.7
0.25	0.080	1.19	58.7	1.483	0.78	50.5	3.6×10^{-4}	2.7	88.8
1.00	0.043	1.28	55.8	5.148	9.8×10^{-4}	35.0	8.1×10^{-4}	2.8	80.5

[a]Reference 8.
[b]Reference 10.
[c]Reference 20.

Determining values for the A and E_a coefficients typically requires fitting experimental data points to a modeled curve and then adjusting A and E_a to give the best fit. To achieve agreement, temperature profiles for several different exposure durations are needed. The three exposure durations reported here are not sufficient for fitting, but we wanted to apply the Arrhenius damage model to our data. Therefore, we took three sets of coefficients reported in the literature and computed the damage predicted for our *in vitro* threshold thermal profiles. The coefficients reported by Welch and Polhamus[8] were measured using an *in vivo* retina model and used the square-wave thermal exposure approximation for long exposures (> 1 s). Simanovskii et al.,[10] used short exposure durations (0.1 s and shorter), where the square-wave approximation cannot be used, and they used NIH 3T3 cells (non-retinal) in culture. We also used the coefficients reported by Moussa et al.,[20] which were obtained using a unique method to expose HeLa S-3 cells to a controlled thermal stress (heated microscope stage) that allows the Arrhenius integral to be evaluated analytically.

For each set of coefficients, we integrated Ω over the duration of each exposure ("Ω at τ") for the threshold mean temperature profiles [Fig. 8(d)] extracted from the boundaries of death (Table 2). In addition, we made a comparison of the degree with which the temperatures at each time point along our thermal profiles needed to be scaled in order to force $\Omega = 1$ at τ. Theoretically, if temperature rise is linearly dependent on the incident laser irradiance (E), then changes in laser power will change only the scale of the temperature rise. Scaling the temperature rise by a constant then is equivalent to scaling the incident laser power,

$$\Delta T(t, \alpha E_0) = \alpha \Delta T(t, E_0). \qquad (2)$$

Table 2 lists the scaling factors (α) required to force $\Omega = 1$ for each of our *in vitro* threshold temperature profiles. In addition, we have multiplied the threshold peak temperature rise values (derived by subtracting 35°C from averaged threshold T_{peak} of two methods in Table 1) by the scaling factors (and adding back the 35°C) to calculate an adjusted T_{peak} value for each scenario. Thus, the adjusted T_{peak} values in Table 2 represent peak temperatures after adjusting entire thermal profiles (without altering shape) to fit each of the three sets of Arrhenius rate coefficients.

The data represented in Table 2 correlate well with expectations when considering the details of the studies used to derive the rate coefficients. First, the adjusted T_{peak} values derived from the Moussa et al.[20] coefficients were substantially greater than the other two sets, which correlates with the very harsh damage endpoints employed for determining damage (thermal bubbling visible with light microscopy). Our calculations show that the coefficients from Simanovskii et al.[10] generated the closest approximation to $\Omega = 1$ for all three exposure durations, and the adjusted T_{peak} values for exposure of 0.1 and 0.25 s were within reasonable limits. As the authors noted in their report,[10] the predictive power of these coefficients seems to be best suited for exposure durations $\leq$ of 1 s because damage is expected to occur at about 37°C. Finally, the "Ω at τ" values determined from the Polhamus rate coefficients were within two to three orders of magnitude of a value of 1, and the corresponding adjusted T_{peak} values turned out to be in a fairly narrow range of 56–61°C. The only condition in which an Arrhenius coefficient set solved for an adjusted T_{peak} within our *in vitro* T_{peak} range (53 ± 1.5°C) was that of Simanovskii et al.[10] 0.25 s, but the general trends of the adjusted T_{peak} values suggests this was likely a coincidence and point toward a lack of overall fit with an exponential rate process model.
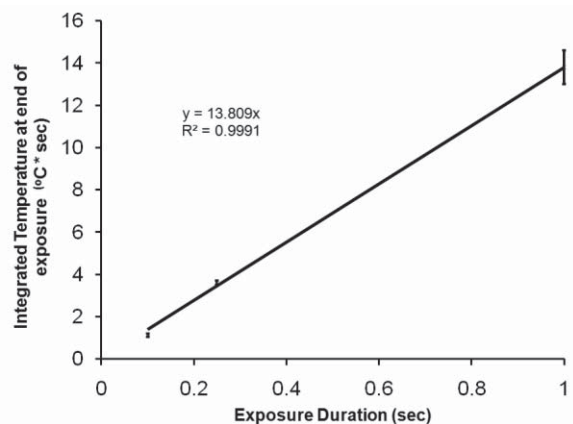
Fig. 9 Dependence of time-integrated temperature on laser exposure duration. The time-averaged integrated temperatures for 0.1–1.0-s exposures were plotted (± standard deviations) against the exposure durations for which they were derived. The slope of the resulting line is a measure of the average temperature of all the exposures.

3.3 Time-Integrated Temperature

Even though T_{peak} for cells at the boundary of cell death (threshold) was found to be the same for laser exposures of 0.1–1.0 s, the shapes of the individual thermal profiles (Fig. 8) were different. Thus, we continued our thermal analysis of cultured cells using the product of temperature and time, or time-integrated temperature (T_{int}). Table 1 provides the T_{int} values for the *in vitro* laser exposures and Fig. 9 illustrates the observed trend between T_{int} and laser exposure duration. Again, we appreciate that our data only represent one order of magnitude between exposure durations but we do assert that the linearity could be significant. Notice that the slope of the line generated in Fig. 9 ($\sim$14 °C) represents a common time-averaged temperature rise for all three exposure durations, and this metric (49 °C) may also show utility in predicting thermally-induced cell death, at least for durations of 0.1–1.0 s and the viability assay we used.

4 Summary

We used a spatiotemporal method in an RPE cell model to map laser damage threshold temperatures at the cellular level for exposure durations of 0.1-s, 0.25-s, and 1.0-s. At the end of each exposure, the mean temperature at the boundary between live and dead cells is considered the damage threshold peak temperature. We were able to reproducibly identify thermal pixels correlating to cells at the boundary of cell death, and we found that the temperature history of these cells were remarkably consistent within each of the exposure durations. The mean threshold temperature profiles at the boundary of cell death for the three exposure durations had different shapes, but achieved the same peak temperature (53ºC) and time-averaged temperature (49°C). We believe that as an adjunct or alternative to the Arrhenius integral, simulating expected laser temperature could lead to assessment of damage for tissues in which threshold peak temperature or time-integrated temperature of the boundary of death has been determined. In addition to utilizing a simpler end point for damage prediction, if temperature is simulated in a spatially-resolved manner, then one will be able to not only predict if the damage "set point" has been reached, it can be used to predict the extent of laser-induced damage within the tissue. In this way, our technique will simplify the prediction of cellular outcomes in heated tissues, such as damage or thermal tolerance, and provide immediate feedback during thermotherapeutic applications.[4,21]

We were surprised that our data do not follow the common single-process rate model (Arrhenius) when used to estimate thermal damage from laser exposures of 0.1–1.0 s. Additional studies, characterizing the kinetics of the damage response to short photothermal exposures, are needed to formulate new hypotheses and computational models that describe the damage rate processes evident in our *in vitro* retinal model. Although cells receiving threshold thermal doses and greater are destined to die, cells outside of the boundary of death are expected to have temperature-dependent heat shock responses[5,6,21,22] that may trigger delayed death,[23] oncogenesis,[24] or even protective adaptive responses.[25] In addition, microthermography in cell cultures could provide thermal dose-response assessments for efficient killing in selective photothermal therapy regimes using aptamer-conjugated nanoparticles,[26]

reducing the number of research animals required in preclinical trials.

Spatial microthermography during exposure to directed energy sources of all kinds, correlated with any image (spatially-resolved effect) taken from a cellular response assay, would provide direct relationships between thermal cause and effect that is unparalleled at present. As the method finds applicability in the life sciences, the types of assays that may be correlated with thermal history include viability and apoptosis staining, immunohistochemical localization of proteins, fusion proteins in gene expression studies, *in situ* hybridization of ribonucleic acid, and even laser-capture microdissection of specific cells visualized by microscopy. These potential applications would result in characterizations of a broad range of relationships between directed energy dose and metabolic response.

References

1. J. R. Mourant, T. M. Powers, T. J. Bocklage, H. M. Greene, M. H. Dorin, A. G. Waxman, M. M. Zsemlye, and H. O. Smith, "*In vivo* light scattering for the detection of cancerous and precancerous lesions of the cervix," *Appl. Opt.* **48**(10), D26–D35 (2009).
2. R. Weissleder, and M. J. Pittet, "Imaging in the era of molecular oncology," *Nature* **452**, 580–589 (2009).
3. K. R. Diller, and J. A. Pearce, "Issues in modeling thermal alterations in tissues," *Ann. NY Acad. Sci.* **888**, 153–164 (1999).
4. B. Kateb, V. Yamamoto, C. Yu, W. Grundfest, and J. P. Gruen, "Infrared thermal imaging: a review of the literature and case report," *NeuroImage* **47**(Suppl. 2), T154–T162 (2009).
5. M. N. Rylander, Y. Feng, J. Bass, and K. R. Diller, "Thermally induced injury and heat-shock protein expression in cells and tissues," *Ann. N.Y. Acad. Sci.* **1066**, 222–242 (2005).
6. M. N. Rylander, Y. Feng, J. Bass, and K. R. Diller, "Heat shock protein expression and injury optimization for laser therapy design," *Lasers Surg. Med.* **39**, 731–746 (2007).
7. G. D. Polhamus, and A. J. Welch, "Effect of pre-exposure fundus temperature on threshold lesion temperatures in the laser-irradiated rabbit retina," *Invest. Ophthalmol.* **14**, 562–565 (1975).
8. A. J. Welch and G. D. Polhamus, "Measurement and prediction of thermal injury in the retina of Rhesus monkey," *IEEE Trans. Biomed. Eng.* **BME-31** 633–644 (1984).
9. S. A. van Nimwegen, H. F. L. Eplattenier, A. I. Rem, J. J. van der Lugt, and J. Kirpensteijn, "Nd:YAG surgical laser effects in canine prostate tissue: temperature and damage distribution," *Phys. Med. Biol.* **54**, 29–44 (2009).
10. D. M. Simanovskii, M. A. Mackanos, A. R. Irani, C. E. O'Connell-Rodwell, C. H. Contag, H. A. Schwettman, and D. V. Palanker, "Cellular tolerance to pulsed hyperthermia," *Phys. Rev. E* **74**, 011915 (2006).
11. R. D. Peters, E. Chan, J. Trachtenberg, S. Jothy, L. Kapusta, W. Kucharczyk, and R. M. Henkelman, "Magnetic resonance thermometry for

predicting thermal damage: an application of interstitial laser coagulation in an *in vivo* canine prostate model," *Magn. Reson. Med.* **44**, 873–883 (2000).

12. D. O. Lapotko, and V. P. Zharov, "Spectral evaluation of laser-induced cell damage with photothermal microscopy," *Lasers in Surg. Med.* **36**, 22–30 (2005).

13. B. Choi, J. K. Barton, E. K. Chan, and A. J. Welch, "Imaging of the irradiation of skin with a clinical CO_2 laser system: Implications for laser skin resurfacing," *Lasers Surg. Med.* **23**, 185–193 (1998).

14. C. Li, D. E. Protsenko, A. Zemek, Y-S Chae, and B. Wong, "Analysis of Nd:YAG laser-mediated thermal damage in rabbit nasal septal cartilage," *Lasers Surg. Med.* **39**, 451–457 (2007).

15. M. L. Denton, M. S. Foltz, K. J. Schuster, G. D. Noojin, L. E. Estlack, and R. J. Thomas, "*In vitro* model that approximates retinal damage threshold trends," *J. Biomed. Opt.* **13**, 054014 (2008).

16. M. L. Denton, C. D. Clark III, Michael S. Foltz, K. J. Schuster, G. D. Noojin, L. E. Estlack, and R. J. Thomas, "*In vitro* model reveals a sharp transition between laser damage mechanisms," *J. Biomed. Opt*. **15**, 030512 (2010).

17. G. Schuele, M. Rumohr, G. Huettmann, and R. Brinkmann, "RPE damage thresholds and mechanisms for laser exposure in the microsecond-to-millisecond time regimen," *Invest. Ophthalmol. Vis. Sci.* **46**, 714–719 (2005).

18. M. H. Niemz, *Laser-Tissue Interactions: Fundamentals and Applications* (Springer, New York 2007).

19. J. Pearce and S. Thomsen, "Rate process analysis of thermal damage," in *Optical-Thermal Response of Laser-Irradiated Tissue*, A. J. Welch and M. J. C. van Gemert, Eds., pp. 561–606, Plenum Press, New York (1995).

20. N. A. Moussa, J. J. McGrath, E. G. Cravalho, and P. J. Asimacopoulos, "Kinetics of thermal injury in cells," *J. Biomech. Eng.* **99**, 155–159 (1977).

21. Y. Feng, J. T. Oden, and M. N. Rylander, "A two-state cell damage model under hyperthermic conditions: Theory and *in vivo* experiments," *J. Biomech. Eng.* **130**, 041016 (2008).

22. G. J. Wilmink, S. R. Opalenik, J. T. Beckham, J. M. Davidson, and E. D. Jansen, "Assessing laser-tissue damage with bioluminescent imaging," *J. Biomed. Opt.* **11**, 041114 (2006).

23. J. T. Beckham, M. A. Mackanos, C. Crooke, T. Takahashi, C. O'Connell-Rodwell, C. H. Contag, and E. D. Jansen, "Assessment of cellular response to thermal laser injury through bioluminescence imaging of heat shock protein 70," *Photochem. Photobiol.* **79**, 76–85 (2004).

24. C. Jolly, and R. I. Morimoto, "Role of the heat shock response and molecular chaperones in oncogenesis and cell death," *J. Natl. Cancer Inst.* **92**, 1564–1572 (2000).

25. E. J. Calabrese, "Converging concepts: adaptive response, preconditioning, and the Yerkes-Dodson law are manifestations of hormesis," *Aging Res. Rev.* **7**, 8–20 (2008).

26. G. S. Terentyuk, G. N. Maslyakova, L. V. Suleymanova, N. G. Khlebtsov, B. N. Khlobtsov, G. G. Akchurin, I. L. Maksimova, and V. V. Tuchin, "Laser-induced tissue hyperthermia mediated by gold nanoparticles: toward cancer phototherapy," *J. Biomed. Opt.* **14**, 021016 (2009).